

Excitonic structure of the optical conductivity in MoS₂ monolayers

Emilia Ridolfi,¹ Caio H. Lewenkopf,² and Vitor M. Pereira^{3,1,*}

¹Centre for Advanced 2D Materials, National University of Singapore, 6 Science Drive 2, Singapore 117546

²Instituto de Física, Universidade Federal Fluminense, 24210-346 Niterói, Brazil

³Department of Physics, National University of Singapore, 2 Science Drive 3, Singapore 117542

(Dated: May 28, 2018)

We investigate the excitonic spectrum of MoS₂ monolayers and calculate its optical absorption properties over a wide range of energies. Our approach takes into account the anomalous screening in two dimensions and the presence of a substrate, both cast by a suitable effective Keldysh potential. We solve the Bethe-Salpeter equation using as a basis a Slater-Koster tight-binding model parameterized to fit the *ab initio* MoS₂ band structure calculations. The resulting optical conductivity is in good quantitative agreement with existing measurements up to ultraviolet energies. We establish that the electronic contributions to the C excitons arise not from states at the Γ point, but from a set of \mathbf{k} -points over extended portions of the Brillouin zone. Our results reinforce the advantages of approaches based on effective models to expeditiously explore the properties and tunability of excitons in TMD systems.

PACS numbers: 72.80.Ga, 71.35.Cc, 11.10.St

I. INTRODUCTION

The widespread availability of bulk trigonal molybdenum disulfide (MoS₂) has made this material one of the most widely studied transition metal dichalcogenides (TMDs) — especially at the strict monolayer thickness —, and has propelled MoS₂ to one of the most prominent members of the family of semiconducting two-dimensional materials beyond graphene^{1–5}. In parallel with the interest and continued advances in optimizing sample production and transport characteristics, MoS₂ and other closely related TMDs are of great appeal for optoelectronic applications^{1,4,5}. This has sustained intensive research to understand the processes that govern the electronic response of these crystals to light. Much progress has been made theoretically^{6–22} and experimentally^{12,17,23–42} in both understanding fundamental properties and exploring the potential practical uses of these materials in devices.

As in nearly all strictly two-dimensional materials, MoS₂ monolayers have a highly tunable carrier density^{3,43–45} and are amenable to having a number of properties tailored on-demand by different external procedures, including the customization of the optical band-gap⁴⁶. It was early recognized that the intrinsic two-dimensionality and semiconducting character of TMDs bring about enhanced Coulomb interactions which, not only renormalize the electronic band structure with quantitative consequences for all derived single-particle processes, but also give rise to the strongest excitonic effects seen to date in the optical response of semiconductors^{47–49}. With binding energies as high as 0.22 – 1.1 eV^{6,7,9–15,26,30–32,34} (depending on the strength of the interaction due to the sensitivity to their environment) and carrying a large spectral weight^{10,23,27}, these two-particle excitations determine and dominate the optical response of TMD materials. As a result, excitons are now understood as a critical ingredient in any reli-

able theory and model of the optical properties of TMDs, to the extent that any theory that does not account for excitonic effects fails to capture even the most basic qualitative features of the optical gap and/or spectral weight distribution.

Monolayers of semiconducting TMDs are also interesting due to a number of other fundamental and unique features of their electronic structure that can broaden their range of applicability in optoelectronics. For example, the strong spin-orbit (SO) coupling splits the valence bands at the K point by a large amount (Δ_{SOC}) which generates two families of excitons²⁹ [see A and B excitons in Fig. 1(b)] and allows the selective excitation of electrons with predefined spin polarization⁵⁰. Moreover, the non-zero Berry curvature offers a number of opportunities to explore applications related to the non-trivial topological nature of electronic states near the band edges. These include the facile injection of valley-polarized carriers by optical pumping^{51–54}, the ability to control spin and valley populations simultaneously as a result of the spin-valley locking⁵⁵, or the anomalous splitting of bound excitonic levels due to a pseudo spin-orbit coupling of topological origin^{56,57}.

In view of this, the development of reliable models with enough flexibility to allow the prediction of the optical response of TMDs in different experimental settings is clearly of high interest. Ideally, one wishes a scheme that augments the reach and expediency of accurate and unbiased first-principles calculations of the full excitonic spectrum. The latter are notoriously demanding from the numerical point of view and, in addition, are particularly onerous for 2D materials when reasonable convergence is required^{10,58}. It then becomes prohibitive to rely only on these approaches to scan a potentially large scope of modifications (structural, chemical, electronic) that can be of interest to tailor the material's intrinsic response for specific purposes.

In this paper our focus are single-layer systems. Hence-

forth, except if explicitly emphasized otherwise, we shall refer to the MoS₂ monolayer as simply MoS₂. The approach that we describe here begins with an accurate Slater-Koster (SK) tight-binding parameterization of the target band structure⁵⁹. The model parameters are benchmarked against information from first-principles calculations and experiments to describe the most important spectral features of MoS₂, such as the correct energies and orbital content of the low lying conduction and valence bands at the critical points in the Brillouin zone (BZ). We are able to reproduce optical absorption spectra obtained experimentally with quantitative accuracy in both frequency and absolute magnitude. As expected, our calculations agree with previous theoretical works^{6,9,10,31,60} that provide a good description of the strongly localized *A* and *B* excitons. By using a large sampling of *k* points in the Brillouin zone we are also able to study the so-called C-exciton¹⁰ and establish its nature, a subject under debate in the literature^{10,28,31,33}.

The remainder of this paper is organized as follows: In Sec. II we discuss the state-of-the-art experimental and theoretical work on the optical response of TMD monolayers. Section III presents our solution of the BSE using a SK Hamiltonian optimized for MoS₂ monolayers and its use in calculating the optical conductivity in linear response. The results, with focus on the nature of the resonant C excitons, are discussed in Sec. IV. Finally, a summary of our main findings is presented in Sec. V. The paper also includes one appendix that addresses technical issues, such as the choice of the number of bands taken in the calculation, an analysis of the spin-orbit effects in the optical response, and a comparison between the energy spectrum obtained with and without the Coulomb interaction.

II. EXCITONS IN THE OPTICAL RESPONSE OF MOS₂

The optical conductivity, absorption, and reflectance spectra of few and single-layer MoS₂ has been extensively studied in recent experiments^{12,23–33}. It is well established that the onset of optical absorption in clean, undoped monolayers occurs at 1.8 ± 0.1 eV, as measured spectroscopically by reflection and photoluminescence^{12,23,24,27,31,32}, absorption^{26–28,33}, photoemission²⁹, and second-harmonic analysis^{35,38,39}.

The absorption threshold is characterized by two peaks separated by 145 ± 4 meV²⁹, associated with the two families of excitons (*A* and *B*) derived from transitions between the spin-split valence and conduction bands. Studies of angle-resolved photoemission spectroscopy¹², as well as X-ray photoemission and scanning tunneling microscopy/spectroscopy³⁴, show that the single-particle gap lies within 2.15 – 2.35 eV, thereby placing the binding energies of the lowest *A* exciton at 0.22 – 0.42 eV (we note that the non-negligible temperature dependence of the absorption peaks is an important factor when ex-

tracting binding energies and identifying experimental variability^{17,61–63}). Such large binding energy values imply unusually small exciton radii, typically on the order of ~ 5 Å¹³, but still of the Wannier-Mott type.

Theoretically, the solution of the BSE from first principles on the basis of GW-corrected electronic states captures accurately the experimental behavior related to the *A* and *B* excitons^{6,9,10,31,60}. Yet, they also reveal the numerical challenges intrinsic to a full *ab-initio* approach to this problem in 2D systems, which is particularly demanding⁶⁴ in terms of convergence at both the stage of the GW single-particle corrections and the subsequent solution of the BSE^{9,10,31,58,60,65}. Effective models, on the other hand, must cope with the non-Coulomb form of the screened potential which is essential to capture the correct bound exciton series^{66–68}, but prevents closed-form analytical results for the binding energies or wave functions. *k*·*p* models that describe the conduction and valence valleys in terms of a massive Dirac equation adapted to MoS₂^{9,14,26,50} have been able to capture the bound excitonic series^{9,14,26}, the momentum dispersion of the excitonic spectrum¹³, and the excitonic contributions to the optical conductivity^{15,26,50}. A prevalent characteristic of studies based on these models is their focus on specific features, most notably the energy spectrum itself which is non-hydrogenic^{16,57,66} and had not been correctly described until recently. Whereas such a restricted analysis is an implicit requirement of effective mass approaches, it is not a limitation for models based on TB, which can describe the entire BZ and large energy ranges of relevance for experiments and applications, provided the starting Hamiltonian gives a quantitatively accurate and qualitatively faithful description of the single-particle states. Parametrized models, both of the SK type as well as simpler, orbital non-specific TB Hamiltonians, have also been employed with different levels of accuracy and reproducibility of experiments^{7,11,13,15}: some report results on restricted energy ranges around the *A* and *B* peaks^{7,13}, others resort to TB models with a large number of fitting parameters (e.g., > 28)^{11,13} or include only a basis of *d* orbitals^{13,15} (the orbital character becomes relevant away from the *K* point; for example, Ref. 10 identifies the C excitons with states that have both Mo *d*_{z²} and S *p*_{*x,y*} character). Most importantly, the single particle band structure of some of these calculations does not capture well the GW-corrected band gap¹³ or the dispersion of the upper conduction bands¹⁴, which is especially relevant factors in the excitonic problem.

We note, finally, that, due to the zero crystal momentum involved in the underlying electronic excitations, the excitonic fingerprints in the optical properties of bulk MoS₂ are qualitatively and quantitatively similar to those of the monolayer. This follows from the layered structure of the former which, combined with a relatively weak inter-layer electronic coupling, makes the electronic properties of the bulk strongly two-dimensional in character. Not surprisingly, and despite the different screening en-

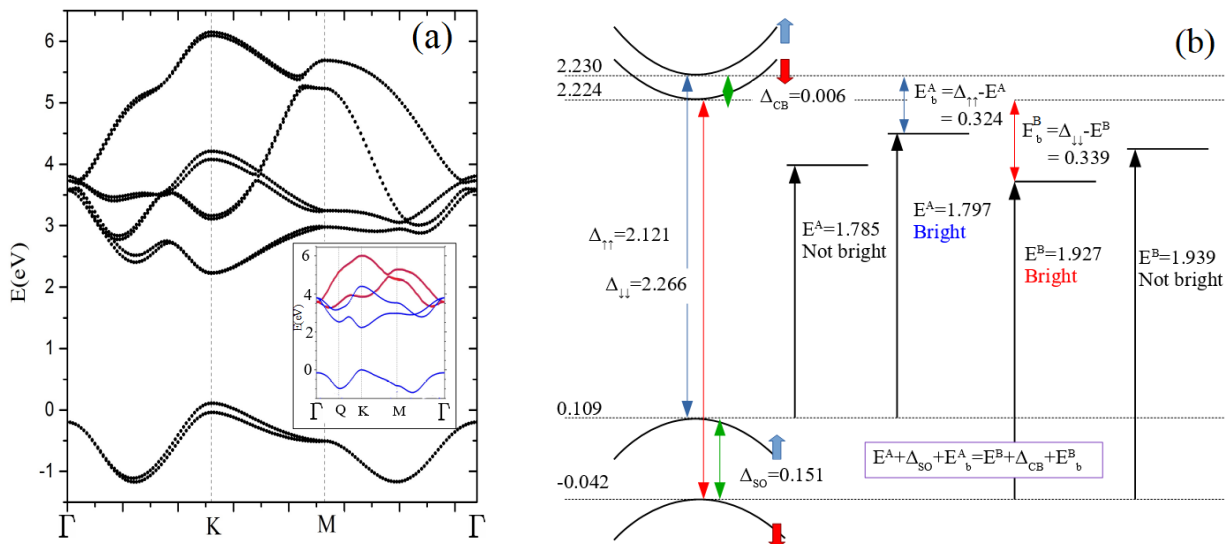


FIG. 1. (a) The reference band structure (including SO coupling) of the MoS₂ monolayer according to the Slater-Koster parameterization discussed in the text and reported earlier in Ref. 59. The full model Hamiltonian can be decoupled into odd and even blocks according to symmetry with respect to the Mo plane (z -reflection symmetry). The inset shows the band structure (without SO coupling) with even (odd) bands highlighted in blue (red) color. (b) Schematic (not to scale) representation of the energy dispersion in the vicinity of the fundamental gap and various energy scales related to our excitonic spectrum, including the optical bandgaps derived from each exciton series ($E^{A,B}$) and the exciton binding energies ($E_b^{A,B}$). This panel deliberately exaggerates the 6 meV splitting of the conduction bands due to SO coupling, in order to make clear the origin of two different excitation energies for each series in our results [e.g., E^A bright and not bright in Fig. 3(a)]. The experimental A and B peaks correspond to E^A (bright) and E^B (bright), respectively, and the represented quantities are related through $E^A + \Delta_{SOC} + E_b^A = E^B + \Delta_{CB} + E_b^B$.

vironment, excitons in bulk samples tend to have binding energies and radii similar to those occurring in the monolayers⁶⁹, and remain mostly localized within one layer⁸. Understanding the excitonic physics in the monolayer is therefore key for the description of the corresponding physics in the bulk as well.

III. THEORY AND METHODS

A. Exciton states and the BSE

Neutral excitations in crystals, both bound and extended, are well described by approximate solutions of the BSE^{58,70–73}. First principles methods have been widely used to investigate the optical properties of insulators and semiconductors in this framework, and provide the current standard to tackle the excitonic spectrum of solid-state materials⁵⁸. Since Coulomb interactions and screening are the essence of the exciton problem, these have to be properly handled in a consistent way to establish even the “single-particle” ground-state of the system (i.e., its one-particle band structure). This need to self-consistently account for quasiparticle corrections in addition to solving the BSE proper constitutes a notable challenge both in terms of implementation and in computational time. Thorough and converged first-principle calculations of the excitonic spectrum and related observ-

ables in MoS₂ have, as a result, been typically few and far between^{9,10,31,60}.

Since the excitonic physics is essential to describe the optical response of semiconducting TMDs, and in view of the current need for accurate, yet expedite, methods to tackle these properties, we solve the BSE and calculate the optical conductivity using an orthogonal SK TB Hamiltonian parameterized to describe the MoS₂ band structure. The atomic orbital basis comprises the three p valence orbitals in each S plus the five d orbitals in each Mo within the trigonal unit cell, giving a total of 11 atomic orbitals. The construction of the Hamiltonian and optimization of its SK parameters has been presented in detail elsewhere⁵⁹. In brief, its main characteristics are: (i) only 14 fitting parameters, (ii) the correct band gap of 2.115 eV at the K point, (iii) the spin splitting of the VB at the K point by 150 meV, (iv) the effective masses and positions of the conduction and valence bands at K , Γ and at the so-called Q point. The TB parameters for the SO coupling have been chosen to match Δ_{SOC} with the experimental energy difference between A and B peaks²⁹. The associated band structure is reproduced in Fig. 1(a), reflecting the insulating ground state of a pristine monolayer. The Bloch states, $\psi_{n\mathbf{k}}(\mathbf{r})$, derived from this Hamiltonian are taken as a good approximation to the eigenstates of the crystal Hamiltonian,

$$\hat{H} \psi_{n\mathbf{k}}(\mathbf{r}) = \varepsilon_{n\mathbf{k}} \psi_{n\mathbf{k}}(\mathbf{r}), \quad (1)$$

where

$$\psi_{n\mathbf{k}}(\mathbf{r}) = \frac{1}{\sqrt{N_c}} \sum_{\mathbf{R}} e^{i\mathbf{k}\cdot\mathbf{R}} \sum_{\alpha} C_{\alpha,\mathbf{k}}^n \phi_{\alpha}(\mathbf{r} - \mathbf{R} - \mathbf{t}_{\alpha}). \quad (2)$$

The lattice vector \mathbf{R} runs over all N_c unit cells of the crystal, n is the band index, α denotes the orbitals, and \mathbf{t}_{α} corresponds to the position in the unit cell of the atoms at which the orbitals are centered. Both the band n and orbital α indices run over the same interval $[1, N]$, where $N = 22$ (11×2 , with spin) is the dimension of the orbital basis considered in the SK Hamiltonian. These Bloch states are used to set up the BSE in the Tamm-Dancoff approximation (TDA) by introducing a basis of two-particle excitations of the Fermi sea, $|\text{FS}\rangle \equiv \prod_{v\mathbf{k}} a_{v\mathbf{k}}^{\dagger} |0\rangle$,

$$|v\mathbf{k} \rightarrow c\mathbf{k}\rangle \equiv a_{c\mathbf{k}}^{\dagger} a_{v\mathbf{k}} |\text{FS}\rangle. \quad (3)$$

The latter are used to express the exciton states

$$|M\rangle = \sum_{c,v,\mathbf{k}} A_{cv\mathbf{k}}^M |v\mathbf{k} \rightarrow c\mathbf{k}\rangle, \quad (4)$$

with energy E_M , where M labels the excitonic modes.

Note that these definitions implicitly restrict the exciton momentum to zero; this is sufficient to capture all first order optical processes, as the excitons with zero momentum are the optically bright ones. Hence, we restrict our discussion to this subspace only. Furthermore, we employ the traditional notation “ c/v ” to designate conduction and valence bands in order to emphasize that we shall be working at zero temperature. It is also instructive to note at this point that, since $c \in [1, N_c]$, and $v \in [1, N_v]$ where N_c/N_v is the number of conduction/valence bands, the dimension of the vector space spanned by the basis states in Eq. (3) is $N_{\text{tot}} \equiv N_k^2 \times N_c \times N_v$, where N_k^2 represents the total number of points sampled in the BZ. The number of bands and the size of the sampling in \mathbf{k} points is one of the critical limiting factors in calculations of the two-particle spectrum, even within a parameterized TB framework.

Replacing (4) in the Schrödinger equation that includes the many-body Coulomb interaction yields the reduced eigenproblem^{11,13,74}

$$E_{cv\mathbf{k}} A_{cv\mathbf{k}}^M + \frac{1}{V} \sum_{c',v',\mathbf{k}'} W_{cv\mathbf{k},c'v'\mathbf{k}'} A_{c'v'\mathbf{k}'}^M = E_M A_{cv\mathbf{k}}^M. \quad (5)$$

Here, $E_{cv\mathbf{k}} \equiv \varepsilon_{c\mathbf{k}} - \varepsilon_{v\mathbf{k}}$ is the energy difference between the c and v bands at \mathbf{k} , $V \equiv A_c N_k^2$ is the total area of the crystal ($A_c = \sqrt{3}a^2/2$ with $a \simeq 3.16 \text{ \AA}$ the lattice constant) and $W_{cv\mathbf{k},c'v'\mathbf{k}'} \equiv \langle v\mathbf{k} \rightarrow c\mathbf{k} | \hat{U} | v'\mathbf{k}' \rightarrow c'\mathbf{k}' \rangle$ represents the matrix element of the many-body Coulomb potential, \hat{U} , between two particle-hole excitations. In the TDA, there are two contributions to this matrix element: a direct and an exchange term⁷⁵. As pointed out earlier¹³, in an orthogonal basis and in our approximation where the Coulomb interaction is independent of the orbital character of the states involved, the exchange term

does not contribute for zero-momentum excitons. As a result, only the direct Coulomb matrix element remains, which can be expressed simply as^{11,13}

$$W_{cv\mathbf{k},c'v'\mathbf{k}'}^{(d)} = u(\mathbf{k} - \mathbf{k}') I_{c'\mathbf{k}',c\mathbf{k}}^* I_{v'\mathbf{k}',v\mathbf{k}}, \quad (6)$$

where $u(\mathbf{q})$ is the Fourier transform of the *screened* Coulomb potential⁵⁸. The orthogonality assumed in defining our SK basis⁵⁹ allows one to express the overlap integrals $I_{a\mathbf{k}',b\mathbf{k}}$ in terms of the expansion coefficients of the Bloch states (2) as

$$I_{a\mathbf{k}',b\mathbf{k}} = \sum_{\alpha} C_{\alpha\mathbf{k}'}^{a*} C_{\alpha\mathbf{k}}^b. \quad (7)$$

Since the $C_{\alpha\mathbf{k}}^b$ are obtained from the numerical eigenvectors of the Bloch Hamiltonian (2), it is important to ensure a consistent choice of phase because the $I_{a\mathbf{k}',b\mathbf{k}}$ are not gauge-invariant quantities. We chose to require the sum of the basis-set coefficients of the wave function $\rho_{\mathbf{k}}^n = \sum_{\alpha} C_{\alpha\mathbf{k}}^n$ to be real, as suggested in Ref. 58.

B. Screened Coulomb interaction

An accurate approximation to describe the screened Coulomb interaction in Eq. (6) is essential for a realistic description of the excitonic spectrum⁵⁸. Early attempts to theoretically describe the exciton series in MoS₂ and related 2D materials provide a good example of this stringent requirement, since, by simplistically using the bare Coulomb form of the potential, one fails to capture the non-Rydberg level structure observed experimentally^{16,57,66}. The distinct series of bound exciton levels in MoS₂ is due to both its pseudospin degree of freedom¹⁶ and the modified electrostatic interaction in strictly 2D electronic systems which, in Fourier space, acquires the form^{66,67}

$$u(\mathbf{q}) = -\frac{e^2}{2\epsilon_0\epsilon_d q \kappa(q)}, \quad \kappa(q) \equiv 1 + r_0 q, \quad (8)$$

where r_0 defines the 2D polarizability of the electronic system^{65–67} and ϵ_d captures the static, uniform screening due to the top and bottom media surrounding the MoS₂ monolayer¹². We assume a MoS₂ monolayer of effective thickness d and effective dielectric constant ϵ_2 sandwiched between materials with dielectric constants ϵ_1 and ϵ_3 . The environment dielectric constant is thus $\epsilon_d = (\epsilon_1 + \epsilon_3)/2$. The potential (8) has precisely the form derived by Keldysh for a thin metallic film, in which case the parameter r_0 enters as the film thickness⁶⁸. The explicit q -dependence in the dielectric function $\kappa(q)$ due to many-body interactions qualitatively modifies Coulomb’s law in real space which becomes

$$u(\mathbf{r}) = -\frac{e^2}{8\epsilon_0\epsilon_d r_0} \left[H_0\left(\frac{r}{r_0}\right) - Y_0\left(\frac{r}{r_0}\right) \right], \quad (9)$$

where H_0 and Y_0 are Struve and Bessel functions, respectively. The parameter r_0 defines a crossover length scale separating the long-range decay $\propto 1/r$ from the short-range domain characterized by a singularity $\propto \log r$ as $r \rightarrow 0$ ⁶⁵. *Ab-initio* studies have confirmed that the Keldysh interaction accurately describes the screened potential in MoS₂^{9,76}. Thus, we employ $u(\mathbf{q})$ in Eq. (6) to solve the BSE.

Only the parameters r_0 and ϵ_d remain now to fully specify the content of Eq. (5). They have been reported with a large variation among different authors in the recent literature^{9,12-14}. *Ab-initio* calculations of the 2D polarizability find $r_0 \sim 31.2 - 41.5$ Å in vacuum⁹. However, it is known that the precise energy placement of the exciton level series is sensitive to the details of the dielectric environment surrounding the monolayer sample^{13,15,18,46}. Prior estimates for the monolayer in the dielectric environment of an air/substrate interface report values spanning a relatively wide interval, namely, $r_0 \sim 13.55 - 57.6$ Å^{9,12-14}. Since we will be referring to the measurements by Li and collaborators²⁷ as our reference for the experimental optical conductivity, the environment's dielectric constant is $\epsilon_d = 2.5$, as appropriate for the air/silica interface ($\epsilon_1 = 1$, $\epsilon_3 = 4$). In the absence of present *ab-initio* calculations of the corrections to the polarizability due to the effect of a silica substrate, we follow the estimates put forward in Refs. 12 and 13, which are based on the Keldysh-type finite thickness (d) model:

$$r_0 = \frac{2\epsilon_2^2 - \epsilon_1^2 - \epsilon_3^2}{2\epsilon_2(\epsilon_1 + \epsilon_3)} d. \quad (10)$$

In this expression, ϵ_2 stands for an effective dielectric constant of MoS₂. The best agreement with the measured exciton binding energies is obtained with¹² $d \simeq 6$ Å and $\epsilon_2 \simeq 12$ (the latter matches well the results from first principles calculations of the dielectric constant of bulk MoS₂⁹), resulting in $r_0 = 13.55$ Å⁷⁷.

Having thus specified all its contributions, and even though numerically more efficient methods have been proposed recently¹¹, we solved the BSE by full diagonalization of the eigenvalue problem in Eq. (5). In view of the ranges of energy covered in current experiments, we restricted our base states in Eq. (3) to include excitations between $N_v = 2$ valence bands (1×2 since spin is

explicitly included) and $N_c = 8$ conduction bands.

Note that, when considering effective models in the $\mathbf{k} \cdot \mathbf{p}$ (Dirac) approximation it is important to additionally include the pseudospin degree of freedom in the treatment of the effective Schrödinger equation to properly describe the spectrum¹⁶.

C. Optical response

As the D_{3h} point group determines that all rank 2 tensors are in-plane isotropic, in a MoS₂ monolayer it is sufficient to consider the diagonal component of the optical conductivity $\sigma(\omega) \equiv \sigma_{xx}(\omega)$ which is given in linear response by (dipole approximation, $T = 0$)^{11,78}

$$\text{Re } \sigma(\omega) = \frac{e^2 \pi}{m^2 \hbar \omega V} \sum_M |\langle \text{FS} | \hat{P}_x | M \rangle|^2 \delta(\omega - \omega_M). \quad (11)$$

Using Eq. (4) to express $|M\rangle$ we write the total momentum operator matrix element as

$$\langle \text{FS} | \hat{P}_x | M \rangle = \sum_{cv\mathbf{k}} A_{cv\mathbf{k}}^M \langle \text{FS} | \hat{P}_x a_{c\mathbf{k}}^\dagger a_{v\mathbf{k}} | \text{FS} \rangle. \quad (12)$$

Expanding the many-body momentum operator in the usual way, $\hat{P}_x = \sum_{pq} \langle p | \hat{p}_x | q \rangle a_p^\dagger a_q$, one has

$$\langle \text{FS} | \hat{P}_x a_s^\dagger a_r | \text{FS} \rangle = \sum_{pq} \langle p | \hat{p}_x | q \rangle [\delta_{pr} \delta_{qs} f_r (1 - f_s) + \delta_{pq} \delta_{sr} f_p f_s], \quad (13)$$

where f_j corresponds to the Fermi-Dirac occupation number of an electron at the state j . At zero temperature and noting that we are interested in the case where $c \neq v$, we write

$$\begin{aligned} \langle \text{FS} | \hat{P}_x a_{c\mathbf{k}}^\dagger a_{v\mathbf{k}} | \text{FS} \rangle &= \langle \psi_{v\mathbf{k}} | \hat{p}_x | \psi_{c\mathbf{k}} \rangle \\ &= \frac{m}{\hbar} \langle \psi_{v\mathbf{k}} | \nabla_{k_x} \hat{H}(\mathbf{k}) | \psi_{c\mathbf{k}} \rangle. \end{aligned} \quad (14)$$

Hence, inserting here the expression for Bloch states given in Eq. (2), the optical conductivity (11) becomes

$$\text{Re } \sigma(\omega) = \frac{e^2}{4\hbar} \frac{4\pi}{\hbar \omega V} \sum_M \left| \sum_{\mathbf{k}cv} A_{cv\mathbf{k}}^M \sum_{\alpha\beta} (C_{\alpha\mathbf{k}}^v)^* C_{\beta\mathbf{k}}^c \nabla_{k_x} \langle \phi_\alpha | \hat{H}(\mathbf{k}) | \phi_\beta \rangle \right|^2 \delta(\hbar\omega - \hbar\omega_M). \quad (15)$$

This form makes explicit that the oscillator strength associated with each particle-hole excitation involves contributions that depend both on the solution of the BSE (through the eigenvector components $A_{cv\mathbf{k}}^M$) and on the effective Hamiltonian in the crystal momentum representation (through the components $C_{m\mathbf{k}}^c$).

The response in the non-interacting approximation (single-particle) is readily recovered by noting that, in the absence of particle-hole interaction, the BSE, Eq. (5), is diagonal. In this limit, $A_{cv\mathbf{k}}^M \rightarrow \delta_{cv\mathbf{k},M}$, $E_M \rightarrow E_{cv\mathbf{k}}$, and

Eq. (15) simplifies to

$$\text{Re } \sigma_{\text{sp}}(\omega) = \frac{e^2}{4\hbar} \frac{4\pi}{\hbar\omega V} \sum_{cv\mathbf{k}} \left| \sum_{\alpha\beta} (C_{\alpha\mathbf{k}}^v)^* C_{\beta\mathbf{k}}^c \nabla_{k_x} \langle \phi_\alpha | \hat{H}(\mathbf{k}) | \phi_\beta \rangle \right|^2 \delta(\hbar\omega - E_{cv\mathbf{k}}). \quad (16)$$

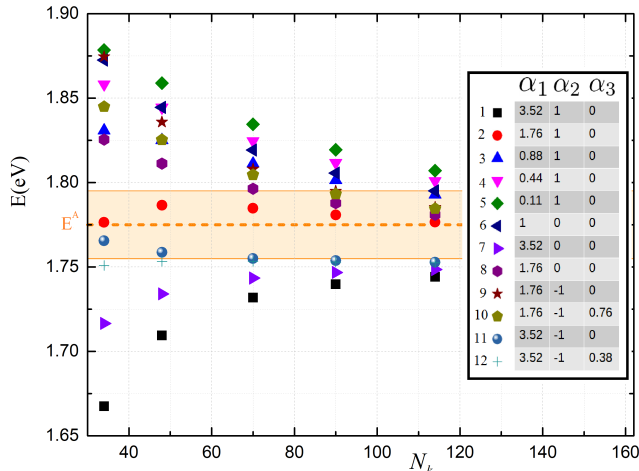


FIG. 2. The energy of the lowest eigenvalue of the BSE [$E^A = 1.775$ eV, dark, cf. Fig. 3(a)] as a function of the total number of \mathbf{k} points used in the uniform sampling of the Brillouin zone. The horizontal dashed line indicates the value obtained from the combined extrapolation of all the curves corresponding to the different regularizations. The shaded strip identifies the energy interval within ± 20 meV of the extrapolated result.

IV. RESULTS

A. Convergence of the exciton spectrum

We solve the eigenproblem in Eq. (5) using a uniform sampling of N_k points along the directions defined by the reciprocal lattice vectors $\mathbf{b}_1 = (2\pi/a, 2\pi/a\sqrt{3})$, $\mathbf{b}_2 = (2\pi/a, -2\pi/a\sqrt{3})$. We place the Γ point at the origin, leaving K and M at the center of our BZ sampling domain [see Fig. 5(a) below]. Since the Coulomb interaction is not periodic in the reciprocal space and our approach does not include local field terms (*i.e.*, Fourier components beyond the first BZ), the selection of the sampling domain can have an impact on the energies of the bound excitonic levels, especially when these arise from transitions at \mathbf{k} points near BZ boundaries. More specifically, in the summation performed in Eq. (5), \mathbf{k}' formally runs over the whole reciprocal space, which can be expressed by defining $\mathbf{k}' \equiv \mathbf{k}'' + \mathbf{Q}$, with \mathbf{k}'' spanning the first BZ and \mathbf{Q} the reciprocal lattice. When the excitonic states have wave functions strongly localized near the edges of the BZ, one must include $\mathbf{Q} \neq 0$ terms, otherwise one misses important contributions from Coulomb matrix elements between \mathbf{k} states closely spaced, but in

adjacent Brillouin zones. Since the wave functions relevant to our problem are localized in regions around the \mathbf{K} points in the BZ (to be discussed below, see Fig. 5), our choice of the \mathbf{k} -domain gives converged results for the excitonic spectrum in agreement with the experiment reported in Ref. 27 by keeping only $\mathbf{Q} = 0$ (*i.e.* by considering all wave vectors and matrix elements within the first BZ). Being able to work with this truncation of the Coulomb matrix elements without affecting the convergence of the spectrum provides an additional improvement in the numerical efficiency of the calculation.

Note, however, that any discrete approach requires the regularization of the \mathbf{k} -diagonal matrix elements $W_{cv\mathbf{k},c'v'\mathbf{k}}$ due to the $\propto 1/|\mathbf{k} - \mathbf{k}'|$ integrable singularity that arises from the long range tail of the screened potential [cf. Eq. (8)]. As their contributions to Eq. (5) become regular in the thermodynamic limit $N_k \gg 1$, this regularization is well posed in the sense that the specific way it is performed has no influence on the calculated observables in that limit. However, we find that the regularization strategy *significantly* impacts the rate of convergence of the spectrum with N_k , to the extent that one can gain an order of magnitude reduction in the dimension of the Bethe-Salpeter matrix for a given convergence target. This is a point of high practical significance because, in an effective SK description such as ours, the number of bands is, by construction, the minimal *a priori* required set. The BZ sampling thus becomes the limiting factor determining the size and tractability of the numerical problem for a given target precision of the calculated spectrum. Since the singular matrix elements are integrated over the \mathbf{k} -space, the most straightforward regularization consists in replacing $u(\mathbf{q} = \mathbf{k} - \mathbf{k}' = 0)$ by its average value over a small enclosing domain $\Delta_{\mathbf{q}}$, namely,

$$u(\mathbf{q} \approx 0) \rightarrow \frac{1}{\Delta_{\mathbf{q}}} \int_{\Delta_{\mathbf{q}}} u(\mathbf{q}) d\mathbf{q} \approx \frac{caN_k}{2\pi} \left[\alpha_1 + \alpha_2 \frac{2\pi r_0}{aN_k} + \alpha_3 \left(\frac{2\pi r_0}{aN_k} \right)^2 \right]. \quad (17)$$

Here, $c \equiv -e^2/2\epsilon_0\epsilon_d$ and the constants α_j depend on the geometry of the averaging domain $\Delta_{\mathbf{q}}$ and the truncation level of the expansion (17).

Fig. 2 illustrates the different convergence rate of the lowest exciton level (E^A) as a function of the sampling dimension. For demonstration purposes, these data were obtained by solving Eq. (5) with only the two bands of each spin nearest to the bandgap (*i.e.*, $N_c = N_v = 2$). The asymptotic value is clearly approached much faster for certain choices of the regularization scheme. In particular, one sees that neglecting the leading higher order

terms in the expansion (17) by having $\alpha_1 = 1$, $\alpha_{2,3} = 0$ (parameter set #6, see label in Fig. 2) provides a particularly slow convergence⁷⁹. This is not unexpected because $2\pi r_0/a \simeq 26.9$, which is precisely of the same magnitude as those values of N_k that are within practical numerical reach⁸⁰. On the other hand, the particular α parameter sets #2 and #11 (see labels in Fig. 2) provide much faster convergence to the asymptotic value $E^A = 1.775$ eV within a 0.020 eV precision⁸¹. This translates into a binding energy $E_b^A = 0.34$ eV since the single-particle gap in our SK band structure parametrization is $E_g = 2.12$ eV⁵⁹ (this value corresponds to the first dark A exciton, while the first bright one has $E^A = 1.80$ eV and binding energy $E_b^A = 0.32$ eV). Henceforth, all our calculations will be presented according to the regularization scheme #2. We have verified that it works efficiently for the whole spectrum.

Fig. 3(a) shows a direct comparison between our BSE-derived eigenvalues and experimental spectra measured for MoS₂ in silica in the range of the single-particle gap^{27,30}. We find that, except for a global rigid offset of 0.07 eV, the spectrum obtained with our model parameters reproduces extremely well the bound exciton series. In particular, it captures with accuracy the level spacing of the lowest-lying states which are those most sensitive to the modified screened potential (9) at short distances and, hence, those that most clearly deviate from a hydrogen-like spectrum^{16,57,66}. This spectrum also captures the fact that the ground excitonic state is dark, as recently established experimentally⁸². We obtain a bright-dark splitting of $\Delta E_{bd} \approx 12$ meV for the lowest excitonic states. This value is due to the 6 meV separation of the conduction bands due to spin-orbit coupling plus differences in effective masses. Our results agree with other theoretical calculations that find $\Delta E_{bd} \lesssim 20$ meV^{83–85} depending on the kind of *ab-initio* approach. So far, the only direct experimental investigation of the bright-dark splitting in MoS₂⁸² finds $\Delta E_{bd} \approx 100$ meV. This value is unexpectedly large in view of the theoretical literature and considering that for TMDs with a larger spin-orbit coupling, like MoSe₂ and WSe₂, one finds $\Delta E_{bd} \approx 47 - 57$ meV^{82,86}. These elements indicate that quantitative aspects of ΔE_{bd} in MoS₂ are still under experimental scrutiny.

To allow a direct comparison of the absorption spectrum with the experiments, a rigid blue-shift in the energies by +0.07 eV has been incorporated in the results shown in Fig. 3. Such a “calibration” is somewhat expected because of the effective parameterizations of both the band structure and the screened Coulomb potential⁸⁷ (yet, a 0.07 eV offset is rather small in comparison with similar approaches, where corrections of up to 0.57 eV were necessary¹³). This calibration of the energy axis has been also applied in the presentation of all our subsequent results.

The bound series is directly associated with transitions between the topmost valence and bottom conduction bands near the K point of the BZ. Each level is 2-fold

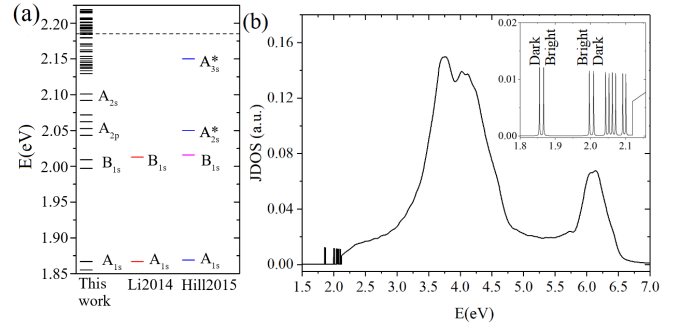


FIG. 3. (a) Comparison of the lower portion of the theoretical exciton spectrum obtained in this work with the energies of the A and B peaks measured in Refs. 27 and 30 (note that the assignment of the peaks labeled A_{2s}^* and A_{3s}^* is not unequivocal in Ref. 30). After a rigid displacement by +0.07 eV (see text), the theoretical spectrum reproduces extremely well the position of the experimental A and B peaks. The dashed horizontal line indicates the one-particle energy gap at 2.18 eV ($2.18 = 2.12 + 0.07$). (b) Joint density of exciton states as defined in Eq. (18), already rigidly displaced by +0.07 eV. A Lorentzian level broadening of 0.1 eV (full width) has been used, except in the lower energy range (magnified in the inset) where it is 0.001 eV to allow the resolution of individual bound exciton levels.

degenerate on account of the $K-K'$ valley degeneracy. When the small energy difference between the two lowest spin-polarized conduction bands at K/K' is ignored, there is an additional 2-fold degeneracy. In our calculations, that small energy difference is explicitly finite [cf. Fig. 1(b)] which explains the existence of two closely spaced levels labeled, for example, A_{1s} , in Fig. 3(a). Nevertheless, one should keep in mind that only half of these excitons are optically bright due to the parity selection rule¹³.

In this respect, it is worth to point out that the difference in the excitation energies of the lowest bound A and B excitons does not follow exactly the spin-orbit splitting of the bands. This is significant because many theoretical TB parameterizations in the literature have identified $E^B - E^A$ directly with the SO coupling parameter and, equivalently, this exciton splitting is frequently used as a direct experimental measure of the spin-orbit splitting in the single-particle band structure, which is not strictly correct. For example, we obtain $E^B - E^A = 130$ meV while the valence band splitting due to SOC in our chosen TB is 150 meV. The difference can be mainly traced back to the different effective masses of the spin-split valence bands⁷.

To identify the \mathbf{k} -point sampling that guarantees convergence of the whole spectrum, we have analyzed the exciton joint density of states (JDOS),

$$\rho_J(E) \equiv \frac{1}{N_c N_v N_k^2} \sum_M \delta(E - E_M), \quad (18)$$

where E_M are the eigenvalues of the BSE. Our calculations show that the JDOS is already reasonably con-

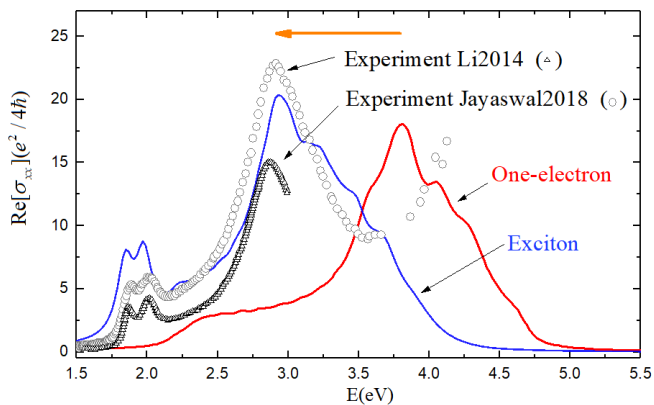


FIG. 4. The room-temperature experimental traces reported in references 27 and 88 for the linear optical conductivity of a MoS₂ monolayer on silica (black) and its comparison with our results with (blue) and without (red) particle-hole interactions ($N_c = 8$, $N_v = 2$, $N_k = 60$). An energy-independent Lorentzian broadening of 0.136 eV (full width) was added to the calculated $\sigma(\omega)$ to capture the experimental broadening at the positions of the A and B excitons. The decay to zero at high energy is artificial: the restricted number of bands used in our diagonalization of the BSE makes the calculated spectra complete only up to ~ 3.5 eV. Nevertheless, for completeness, we show here the conductivity in the full range spanned by those bands.

verged for $N_k = 48$ and that the differences for $N_k = 90$ up to 120 are negligible. We take $N_k = 60$ for the results presented in this paper. The converged JDOS calculated with $N_c = 8$ conduction and $N_v = 2$ valence bands is shown in Fig. 3(b) for $N_k = 60$.

B. Linear optical conductivity

The optical conductivity in linear order is directly obtained from Eqs. (15) and (16) by a diagonalization of the full BSE matrix in the subspace spanned by the 10 bands mentioned above and a suitable sampling of the BZ. The Dirac-delta functions are broadened by replacing them with Lorentzians of full width γ . The latter qualitatively represents a total decay rate due to several microscopic mechanisms, each of them contributing to γ with a characteristic energy dependence¹⁰. Since the experimental broadening is largely disorder and sample dependent, we take the simple approach of considering γ as constant and to adjust its value to fit the experimental data (see discussion below).

Figure 4 shows the real part of $\sigma(\omega)$ that we obtain for the single-particle and BSE calculations. It is our most significant result. For reference, the plot includes the experimental traces reported recently by Li *et al.*²⁷ for exfoliated MoS₂ and Jayaswal *et al.*⁸⁸ for CVD-grown MoS₂, both measured on silica at room temperature. Note that the comparison with experimental data is only meaningful up to ~ 3.5 eV, beyond which excitations involving

additional valence bands not included in our present calculation (Fig. 1a) must be taken into account⁵⁹. We put $\gamma = 0.068$ eV in our calculations, which corresponds to the average width of the A and B exciton peaks reported in the experiment of Li *et al.*. As anticipated, the single-particle results fail to describe the spectral features of the optical response. Even though the discrepancy is most obvious in the region dominated by the bound exciton levels, $E \lesssim 2.1$ eV, there is also a remarkable difference in the continuum. In particular, the single-particle spectral weight is generically distributed at energies much above the interaction-corrected values, as highlighted by the horizontal arrow in Figure 4. Therefore, by neglecting the excitonic effects and interpreting the single-particle absorption spectrum literally, one incurs in a severe qualitative and quantitative misrepresentation, not only in the vicinity of the optical gap, but actually over the entire range of energies. Thus, the strong Coulomb interactions in these two-dimensional materials, not only lead to high exciton binding energies, but also largely renormalize the whole spectrum.

Figure 4 shows that our BSE calculation captures rather well the important experimental features of the optical conductivity in MoS₂, namely, the position of the A and B peaks, the overall maximum at $E^C \simeq 2.85$ eV, the energy dependence over the entire experimental range, and the absolute magnitude of the optical conductivity. We stress that we do not adjust or scale the magnitude of $\sigma(\omega)$, as is frequently done in theoretical work that discusses similar comparisons with experimental data. This overall agreement attests to the validity and accuracy of the SK parameterization of the underlying band structure, and provides strong support to the use of the Keldysh effective screened potential in the BSE calculations (an additional overview of different theoretical and experimental spectra reported in recent literature is given in Fig. 7 of the appendix).

Since γ corresponds to microscopic processes that depend on the excitation energy, one might expect such dependence to have significant influence in the line shape of the optical conductivity. Yet, our calculation that uses a constant broadening captures the measured energy dependence quite satisfactorily. Surprisingly, *ab initio* results^{10,31,60} are less accurate in describing $\text{Re} \sigma(\omega)$ despite the inclusion of specific energy dependent broadening processes, such as electron-phonon scattering¹⁰ [see Fig. 7(b)]. This indicates that the experimental broadening is likely dominated by disorder and justifies *a posteriori* our choice of an energy-independent γ to broaden the numerically discrete spectrum in Eq. (15).

Finally, as pointed out in Ref. 10, convergence studies up to large \mathbf{k} -sampling meshes are essential to guarantee that one meaningfully “reproduces features in the experimental absorption spectrum above 2 eV”. The comparison presented in Fig. 7 provides a good example of how approaches based on parameterized SK models such as ours can outperform full first-principles solutions of the BSE when it comes to expediency and the need of a large

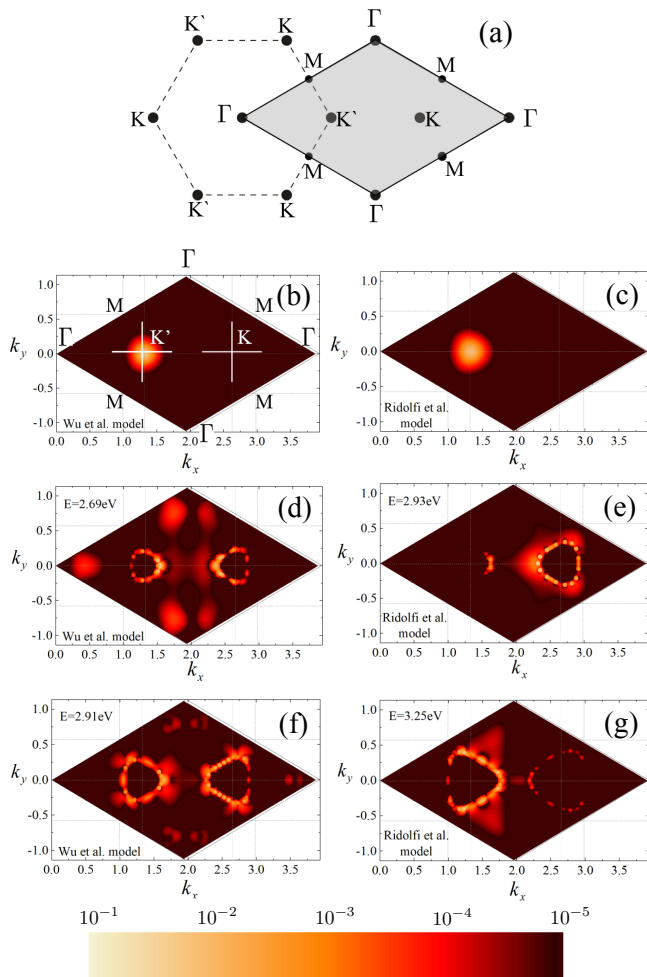


FIG. 5. Representative excitonic wave functions in momentum space including only the two conduction and valence bands closest to E_F ($N_k = 60$, $N_c = N_v = 2$). (a) Diagram of the first BZ of MoS_2 (dashed line) and the equivalent reciprocal unit cell used in our \mathbf{k} -sampling (solid rhombus). The Γ point is located at the vertices of the sampling domain, $M = (\pi/a, -\pi/\sqrt{3}a)$, $K' = (4\pi/3a, 0)$ and $K = (8\pi/3a, 0)$. The left column gives wave functions obtained with the TB model of Ref. 13, while those on the right use the SK parameterization of Ref. 59. The second row [(b) and (c)] shows density plots of the probability distribution arising from one of the wave functions associated with the A peak in the optical conductivity. The two bottom rows [(d) to (g)] show representative wave functions in the region of C excitons. The axes are in units of \AA^{-1} . Note that the color scale is logarithmic.

BZ sampling to ensure convergence. It is key, of course, to rely on underlying band structures that accurately describe the quasiparticle renormalization from the outset.

C. Nature of the C excitons

The maximum in $\text{Re}\sigma(\omega)$ at E^C has been attributed to resonant excitons involving transitions near the center

of the BZ (the Γ point), the so-called C excitons¹⁰. As we discuss below, these excitons are actually not more related to Γ than they are to the K point. Hence, it is incorrect to refer to them as “ Γ -point excitons”. Turning our attention to the spectral details of the conductivity around E^C , Fig. 4 shows that the energy dependence obtained from the excitonic calculation in the interval $[2.5, 3.5]$ eV is nearly identical to that given at the single particle level in the different interval $[3.5, 4.5]$ eV. This seems to indicate that, in this energy range, the primary effect of the electronic interaction is to rigidly redshift the one-electron conductivity by about 0.9 eV, without notable modifications to the line shape (indicated by the horizontal arrow in Fig. 4). That being the case, one could question the attribution of the enhanced spectral weight in this broad region to interaction effects, insofar as (i) the one-electron trace seems to already carry the key aspects of the energy dependence and magnitude of $\sigma(\omega)$ and (ii) the excitonic corrections do not seem to generate any additional spectral feature beyond simply repositioning the curve *en bloc* to lower energies, as expected from the attractive electron-hole interaction. In other words, it appears as if, for excitation energies belonging to the one-particle continuum, the restructuring of the absorption spectrum caused by interactions amounts to a “scissor”-type correction of the energy spectrum, where an effective “binding energy” of ~ 0.9 eV brings the one-electron trace (red) to its correct position (blue), but with essentially no changes in oscillator strength. The problem with this, however, is that the value 0.9 eV is much larger than the binding energy of the A bound excitons ($E_b^A = 0.324$ eV). It turns out that explaining this excitonic redshift on the basis of these one-electron band structure features is questionable and, as we now explain in detail, too simplistic and misleading.

The large spectral weight of the one-electron curve (red in Fig. 4) around its maximum is primarily due to the downward dispersion of the lowest conduction bands along $\Gamma-K$ (see Fig. 1): the fact that conduction and valence bands separated by excitation energies ~ 4 eV disperse roughly parallel to each other entails a large enhancement of the one-particle JDOS in this region, naturally explaining the peak in $\text{Re}\sigma(\omega)$. Equivalently, it can be inferred from Fig. 1 that, in our SK model, the one-electron “optical band structure” is nearly flat along the $\Gamma-K$ line. Hence, the one-electron “C peak” is mostly the result of a large one-electron JDOS at ~ 4 eV (see also Fig. 10 in the appendix which explicitly confirms this).

However, the same conclusion does not apply to the results of the excitonic calculation. As we have seen in Fig. 3(b), the excitonic JDOS is peaked, broadly speaking, at ~ 4 eV while the corresponding conductivity peaks at $E^C \simeq 2.85$ eV. It follows that the enhanced optical response near E^C is, clearly, not the result of a large number of excitonic levels with energies close to E^C . In reality, except for the bound excitonic levels that emerge in the gap, the one-particle and excitonic JDOS do not

differ much at energies in the continuum, as we demonstrate in Fig. 10 (appendix). For example, predicting the spectral shape of the optical conductivity solely on the basis of the excitonic spectrum (through the JDOS) would clearly fail for the energies in the continuum. This is the reason why the idea of an effective “binding energy” of ~ 0.9 eV that rigidly redshifts the one-electron spectrum, as discussed above, is misleading.

We must therefore explicitly consider the oscillator strengths which, according to Eq. (15), are given by

$$\left| \sum_{\mathbf{k}c\nu} A_{c\nu\mathbf{k}}^M \sum_{\alpha\beta} (C_{\alpha\mathbf{k}}^{\nu})^* C_{\beta\mathbf{k}}^c \nabla_{k_x} \langle \phi_\alpha | \hat{H}(\mathbf{k}) | \phi_\beta \rangle \right|^2. \quad (19)$$

Recalling that $A_{c\nu\mathbf{k}}^M$ represents the probability amplitude of the exciton M in reciprocal space, the oscillator strength depends not only on the one-electron dipole matrix elements, but also on the specific texture of each excitonic wave function in \mathbf{k} space.

In Fig. 5 we analyze representative excitonic wave functions in reciprocal space associated with the largest optical spectral weights (cf. Fig. 4 and see also Fig. 6 below). As per our earlier remarks regarding the “calibration” of the energies, the values indicated in each panel are shifted by $+0.07$ eV (right column) and $+0.57$ eV (left column) with respect to the original eigenvalues of the BSE. For reference, Fig. 5(b) and 5(c) show that the wave functions associated with the A and B excitons concentrate at the vicinity of the K points⁸⁹, as has been well established by previous calculations. The degree of their localization is directly related to the large binding energies and, in real space, they appear much more localized than typical excitons in semiconductors^{5,13}. We recall that, due to the parity selection rule, only half of the excitons related to the two valence and two conduction bands straddling the gap are optically bright. Each of the optically bright excitons is 2-fold degenerate on account of the $K-K'$ valley degeneracy (when the small energy difference between the two lowest spin-polarized conduction bands at K/K' is ignored, these are further degenerate with the other pair of doubly-degenerate dark excitons. In our calculations, that small energy difference is explicitly finite, in correspondence with the spectrum shown in Fig. 3).

The picture is rather different for the C excitons. The wave functions shown in panels (d) to (g) of Fig. 5 correspond to selected states with energies close to E^C . We caution the reader that, unlike the case of bound excitons such as A or B, here we show selected representative wave functions of a “continuum” of states. (We have checked over a window of energies near E^C that the spreading of the wave functions over portions of the BZ similar to those shown here is a robust common feature.) Obviously, the two TB models we use^{13,59} render different states. We note, however, the corresponding wave functions show rather large similarities (compare the left and right columns in Fig. 5). Remarkably, there is no pronounced contribution *right at* the Γ point itself; on the contrary, for our choice of primitive cell, the excitonic

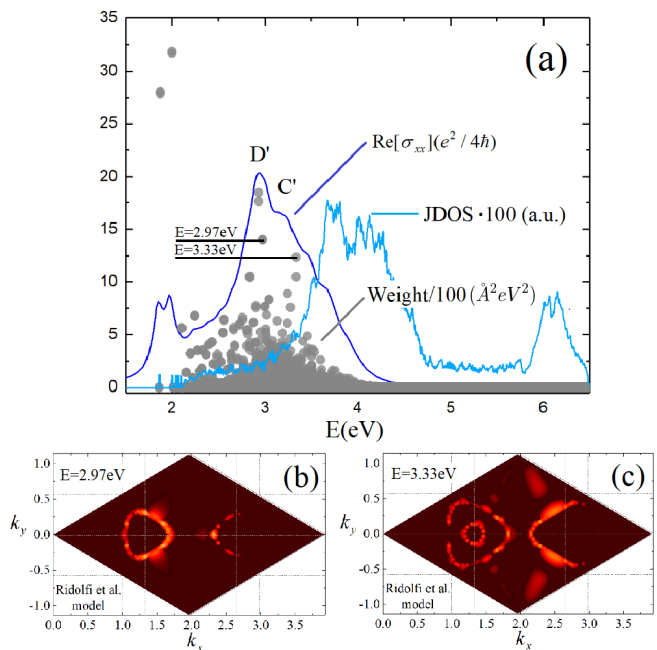


FIG. 6. (a) An overlay of the real part of the optical conductivity, the excitonic JDOS and the oscillator strength expressed in Eq. (19) according to our excitonic calculation. (b) and (c) show representative excitonic wave functions contributing to the peaks D’ and C’ whose energies and spectral weight are highlighted in panel (a). ($N_k = 60$, $N_c = 8$, $N_v = 2$). The axes are in units of \AA^{-1} . Note that the color scale is logarithmic and the same as in Fig. 5.

wave functions appear distributed on a ring at a finite distance from all the symmetry points, midway between $K-M$ and $\Gamma-K$. This agrees with similar observations based on full *ab initio* solutions of the BSE in the region of the C excitons which, likewise, associate C excitons with transitions within a similar annular region, but not specifically at or near Γ ^{10,31,90} (see, for example, Fig. 21 in Ref. 90). Further, the C excitons in Fig. 5 appear as more tightly localized in \mathbf{k} space than their A counterparts, since the rings are rather thin (keep also in mind that the color scale is logarithmic).

This localization is established at a quantitative level by a computation of the inverse participation ratio associated with each exciton wave function, which we describe in the appendix. The data shown there, in Fig. 10(b), reveal that while the region of the C excitons is characterized by a comparatively small JDOS, the corresponding states are typically more localized than the average⁹¹. This ultimately determines the energy dependence of the oscillator strength, which is maximized in the region of energy near E^C , as can be directly seen in Fig. 6 where the quantity (19) is shown for all excitons. Therefore, opposite to the case of a single-particle calculation, the spectral profile of $\text{Re} \sigma(\omega)$ is almost entirely determined by the oscillator strength and not the optical JDOS.

In conclusion, the discussion above indicates that it

is misleading to designate these as “ Γ -point excitons” and reinforces the perspective that relates them with the properties of the “optical band structure” along the $\Gamma-K$ and $K-M$ directions^{10,31}. Extending the calculation of the excitonic wavefunctions shown in Fig. 5 to include not only the lowest 2 but all 8 conduction bands in our TB model, we can conclusively assign the two peaks in the oscillator strength at $E \simeq 2.9$ eV and $E \simeq 3.3$ eV (labeled as D’ and C’ in Fig. 6) to the two contributions distinguished in Ref. 33. Specifically, with our band structure, they arise from particle-hole excitations between approximately parallel bands $\simeq 3.8$ eV apart along the $\Gamma-K$ and $K-M$ symmetry lines. From this point of view, excitons belonging to the broad C region do have a large binding energy of about 0.9 eV ($0.9 = 3.8 - 2.9$). Notably, a comparison between Fig. 5(g) and Fig. 6(c) reveals additional weight in the latter over an inner ring close to K . This is contributed by transitions from the valence to the 5th and 6th conduction bands which disperse downwards and nearly parallel to each other $\simeq 4$ eV apart near K . This vividly illustrates that the attribution of fine details associated with the whole region of the C excitons is sensitive to the particulars of the underlying bandstructure, and necessitates the inclusion of higher conduction bands.

That C excitons arise from particle-hole excitations midway from the $\Gamma-K$ and $K-M$ lines in reciprocal space is consistent with the C peak being more sensitive to the number of layers in thin MoS₂ films than the A and B features. In particular, the experimental shift of E^C correlates with the changes in the separation of bands with MoS₂ thickness^{28,31,92}. These changes in electronic structure are known to be small at the K point but large along the whole $\Gamma-K$ line, ultimately determining the transition from a direct to indirect gap as a function of thickness²⁴. The contrast between A/B and C excitons can be understood from the fact that the electronic states at K/K' contain mostly contributions from the d orbitals in Mo, while in the regions of \mathbf{k} that contribute to the C excitons they have a strong p character arising from the sulfur atoms^{59,90,93}. As d orbitals are spatially more localized and, moreover, lie in the inner of the 3 atomic planes that make each MoS₂ monolayer, the A and B exciton states at K/K' are not as perturbed in a stacked multilayer structure or as a result of strain, in comparison with the changes that occur to the C excitons due to their strong sulfur orbital content⁹⁰.

V. SUMMARY

We revisited the problem of calculating the excitonic spectrum in the MoS₂ monolayer. It has been shown that many-body effects strongly restructure the optical absorption spectrum over an unusually large range of energies in comparison with the single-particle picture. Our approach accounts for the anomalous screening in two dimensions and for the presence of a substrate, both modeled by a suitable effective Keldysh potential. We solve

the Bethe-Salpeter equation for the interacting electron-hole excitations by using a Slater-Koster tight-binding model parametrized to fit the calculated first-principles band structure of the material. The optical conductivity that emerges captures with good accuracy both the shape and absolute magnitude of the experimental data.

Our calculation does not consider any temperature-induced change in the band structure nor microscopic broadening mechanisms such as those from the unavoidable phonon excitations. Indeed, by solving a temperature-dependent BSE based on first-principles electron and phonon spectra, Molina-Sánchez *et al.*⁶¹ have shown that the electron-phonon coupling is responsible for most of the 40 meV red-shift observed between zero and room temperature⁶³. In addition to this, for quantitative and qualitative accuracy at the microscopic level, one must consider the impact of the thermal expansion in the band structures and, in the case of excitons, the broadening contributed by radiative recombination. Details of such processes are, however, not in the scope of the present work; in many experimental cases, such microscopic details are overwhelmed by disorder-induced broadening. To compare our results with experiments at room temperature, we blue-shifted the calculated optical response spectrum by 70 meV and introduced a phenomenological broadening, as discussed in Sec. IV.

Seeing that our result captures well the experimental spectrum up to ~ 3.5 eV, we relied on the predictions of this model to investigate the effects and characteristics of the so-called C excitons. Notably, we explicitly showed in Fig. 5 that they arise from particle-hole excitations in an annular region of the BZ centered at, but at finite radii from, the K points (maximal contributions arise from regions between $\Gamma-K$ and $M-K$).

The interplay between the texture of the excitonic wave functions and the one-electron dipole matrix elements is responsible for the massive transfer of spectral weight seen in the conductivity when compared with results at the one-electron level (Fig. 4). Our results also suggest a cautionary word when it comes to effective mass descriptions of the MoS₂ band structure, especially if the aim is to describe the optical excitations in the vicinity of E^C . In this case, a model that captures only the band structure at the Γ point will be certainly insufficient for that.

Throughout our analysis, we presented results obtained using two different tight-binding descriptions of the underlying single-particle band structure. This provides an example of the immediate transferability in this approach to study the optical response of other members of the TMD family. In such a case, one can readily use the same orbital basis for the TB model and the only material-dependent input is the corresponding band structure. The generic workflow is the same as the one we have used above: (i) Obtain an *accurate* quasiparticle band structure from first principles, (ii) Determine the parameters of the Slater-Koster TB that most faithfully describe such band structure, and (iii) Solve the BSE in

the eigenbasis of that TB Hamiltonian.

Our analysis of two different TB parameterizations also affords a perspective over some aspects that are robust in this approach and others that depend on fine details of the parameterization. Overall, the accuracy of our results based on the SK model developed in Ref. 59 vividly supports the use of effective models to expeditiously explore the properties of excitons in 2D materials. This work shows it to be a reliable strategy, provided that the starting Hamiltonian faithfully describes the quasiparticle-corrected band structure. These approaches are orders of magnitude faster in CPU time than complete first-principles solutions of the BSE. Such an advantage facilitates properly addressing the optical response of MoS₂ at energies around the C excitons, where a fine sampling of the k -space is necessary. We believe that, due to their intrinsic flexibility to model reliably a variety of conditions such as heterostructures, disorder and strain, effective models open the path for a more comprehensive investigation of the optical properties of TMDs where interaction effects play a fundamental role.

ACKNOWLEDGMENTS

We acknowledge fruitful discussions with P. E. Trevisanutto, V. Olevano, T. G. Pedersen, L. Lima, F. Wu, F. Qu, and M. L. Trolle. E. Ridolfi was supported by the Singapore Ministry of Education under grant number MOE2015-T2-2-059. This work was further supported by the Singapore Ministry of Education Academic Research Fund Tier 1 under Grant No. R-144-000-386-114 and the Brazilian funding agencies CNPq, CAPES, and FAPERJ. Numerical computations were carried out at the HPC facilities of the NUS Centre for Advanced 2D Materials.

APPENDIX

A. Optical conductivity: compilation of theoretical results

Figure 7 gives an overview of different theoretical results for the optical conductivity in MoS₂ found in the literature. Panel (a) compiles TB-based calculations^{11,13,15}, while panel (b) compares *ab initio* results^{10,31,61}.

In the case of the TB model, Fig. 7 shows both the $\text{Re}\sigma(\omega)$ given in Ref. 13 as well as the our BSE calculation using Wu and collaborators¹³ TB parameterization over a wider energy range with a suitable broadening adapted to the experimental traces. Figure 7 indicates that the different theoretical approaches describe roughly the same behavior of $\text{Re}\sigma(\omega)$ around the *A* and *B* peaks⁹⁴. In contrast, the energy dependence and spectral weight in the interval [2.0, 3.0] eV that covers the

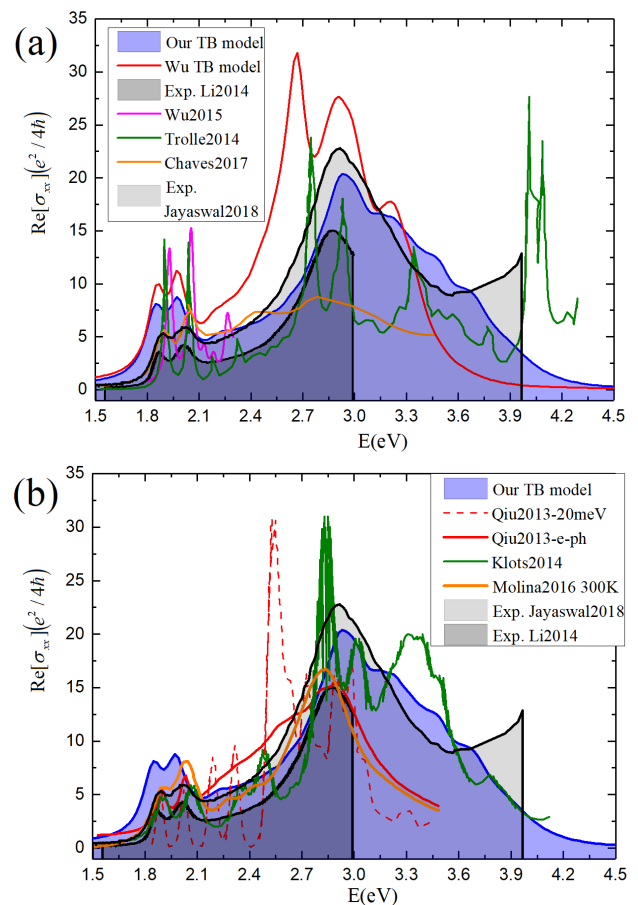


FIG. 7. Comparison between different theoretical predictions for the optical conductivity and the experimental results of Li and collaborators²⁷ and Jayaswal and collaborators⁸⁸. (a) $\text{Re}(\sigma_{xx})$ obtained from the TB-based solutions of the BSE reported in Refs. 11, 13, and 15 contrasted with our calculations based on both the TB model of Ridolfi *et al.*⁵⁹ (blue) and that of Wu *et al.*¹³ (red) (in the latter we added the same broadening indicated in Fig. 4; this curve must be rigidly shifted by +0.57 eV to match the experimental position of the A and B excitons¹³). (b) $\text{Re}(\sigma_{xx})$ based on full *ab initio* solutions of the BSE from Refs. 10, 31, and 61. Since the latter^{31,61} present $\text{Re}(\sigma_{xx})$ in arbitrary units, we vertically scaled each curve to directly compare with the experimental trace. The curve from Ref. 61 is at 300 K.

region of the *C* excitons are significantly approach dependent. In the particular case of the two TB models that we analyze in detail, these differences can be traced to the larger splitting of the conduction bands near the Γ point in the model of Ref. 13 and the different orbital content of the Bloch states that dominate the dipole matrix elements⁹⁵.

B. Number of conduction bands

Reference 10 reports that the C peak is contributed by 6 nearly degenerate exciton states made from transitions

between the highest 2 valence bands and the first three lowest conduction bands (including spin). In Fig. 8 we calculate $\text{Re} \sigma_{xx}$ for $N_c = 2$, $N_c = 6$ and $N_c = 8$ and verify the necessity of including at least $N_c = 6$ bands. We note that the optical conductivity acquires significant corrections due to the increased number of bands precisely in the energy region of the C excitons for both TB models. In the model of Wu *et al.*¹³, the C peak is also slightly enhanced when passing from $N_c = 6$ to 8, while in our TB model the most significant changes occur when passing from 2 to 6.

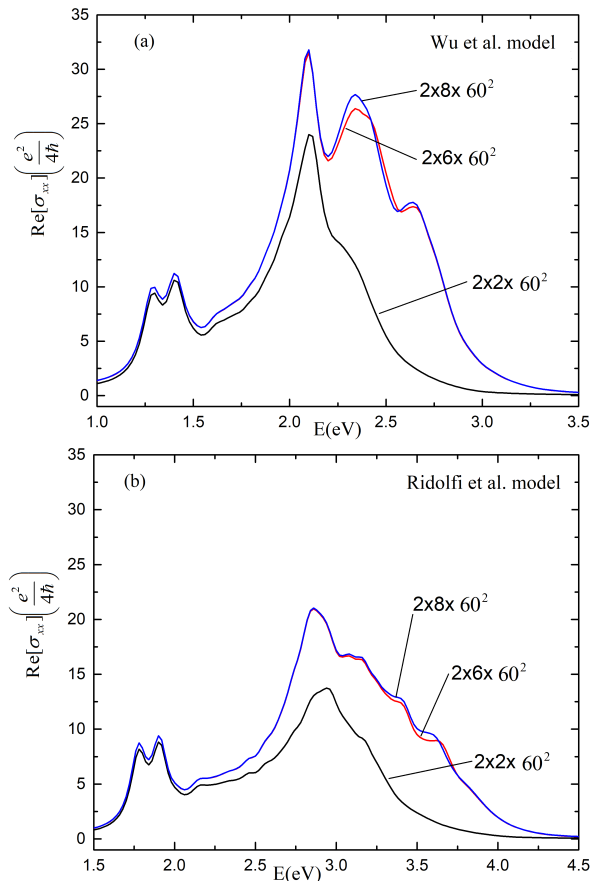


FIG. 8. Linear optical conductivity when considering different numbers of conduction bands in the models of Wu *et al.*¹³ (a) and Ridolfi *et al.*⁵⁹ (b).

C. Even and odd bands

The mirror symmetry with respect to the horizontal plane that contains the transition metal ions has important consequences for the band structure of MoS₂ monolayers. The TB model that we used to describe the ground-state band structure⁵⁹ predicts one even valence band, two even conduction bands, and two odd parity conduction bands around the Fermi energy [see Fig. 1(a)]. The importance of the odd bands has been

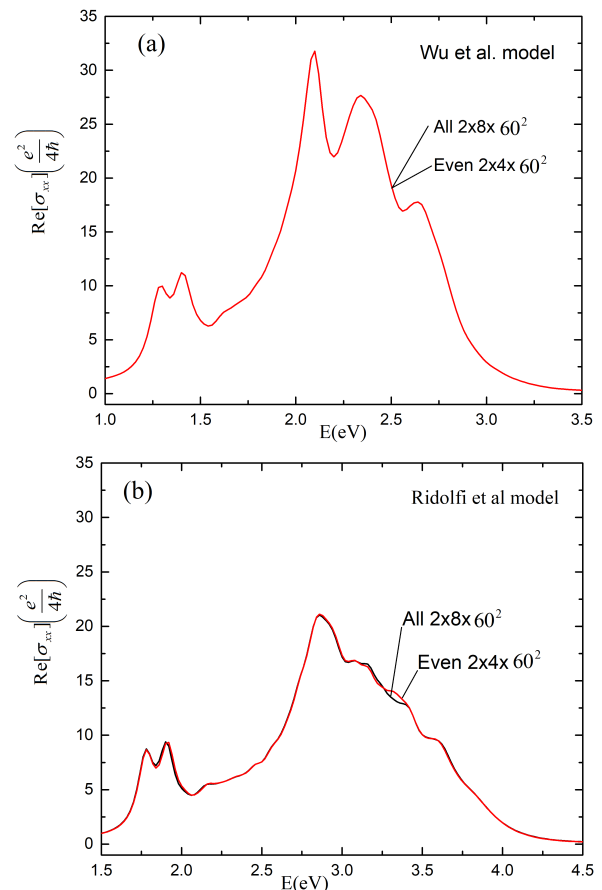


FIG. 9. Comparison between the linear optical conductivity obtained with an “all-band” model ($N_c = 8$, $N_v = 2$, $N_{ks} = 60$) and an “even-band” model ($N_c = 4$, $N_v = 2$, $N_{ks} = 60$) using the TB parameterizations of Wu *et al.*¹³ (a) and Ridolfi *et al.*⁵⁹ (b).

unclear¹⁰, and we examine this issue next.

Figure 9(a) shows that the odd bands of the TB model of Ref. 13 do not contribute to the optical conductivity. This is expected because this TB model does not include spin-flipping terms: since the dipole coupling is diagonal in spin, the non-zero transition matrix elements must involve initial and final states with the same parity under a reflection with respect to the plane. Our TB model gives a small difference between the all even and odd bands basis caused by the coupling of odd and even bands by the spin-flip terms in the Hamiltonian. We conclude that the increment in the optical conductivity when increasing the number of bands comes mainly from the two upper “even” bands.

D. Exciton and one-electron JDOS

When interpreting the origin of the spectral weight shift in the optical conductivity associated with the C excitons, it is useful to analyze how the excitation spec-

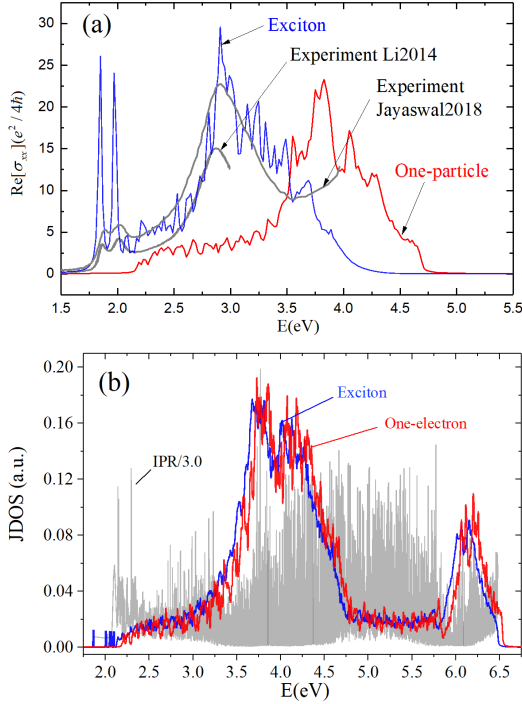


FIG. 10. (a) The same as Fig. 4, except that the calculated curves have been broadened by the smaller value 0.03 eV (full width). (b) Joint density of exciton states (JDOS) as defined in Eq. (18). A Lorentzian level broadening of 0.01 eV (full width) has been used, except in the lower energy range, where we used 0.001 eV to allow the resolution of individual bound exciton levels. The inverse participation ratio (IPR) has been calculated from Eq. (20) and is presented without any broadening.

trum itself changes in the presence of the Coulomb interaction. Fig. 10(a) shows the same data for $\text{Re } \sigma(\omega)$ that was presented in Fig. 4, but using a considerably smaller broadening to reveal more clearly the fine spectral structure. In Fig. 10(b) we compare the joint density of states

(JDOS) with and without interaction. Apart from the emergence of the bound excitonic states in the gap, we can see that the excitation spectrum largely maintains the JDOS computed at the one-electron level. The interaction causes a global redshift of about 0.1 eV, which is much smaller than the spectral weight transfer seen in the conductivity. This figure additionally includes the inverse participation ratio (IPR) of all the excitonic levels (20), which quantifies the degree of localization of the respective wave functions in reciprocal space.

E. Exciton inverse participation ratio

To have an overall perspective over the degree of localization of each exciton's wave function, we computed the inverse participation ratio (IPR),

$$\mathcal{P}(E_M) \equiv \sum_{c\mathbf{k}} |A_{c\mathbf{k}}^M|^4 / \sum_{c\mathbf{k}} |A_{c\mathbf{k}}^M|^2, \quad (20)$$

for all the eigenfunctions of the BSE (5). This quantity provides a rough measure of the spread (in *reciprocal* space) of the wave function belonging to the exciton with energy E_M , being largest for the most localized states and scaling $\propto 1/N_{\text{tot}}$ for states uniformly extended over the whole BZ. The result is included in Fig. 10(b). It reveals that while, on the one hand, the region of the C excitons is characterized by a comparatively small JDOS, on the other, states there are typically more localized than the average, as revealed by a number of peaks of the IPR in the interval [2.75, 3.25] eV. This simply reflects what has been inferred from the selected wave functions shown in Fig. 5 and, moreover, confirms our earlier statement that C excitons are considerably more localized than bound ones in reciprocal space: $\mathcal{P}(E \approx E^{A,B}) \ll \mathcal{P}(E \approx E^C)$. This, of course, is as expected because the latter are true bound states in *real* space (in relation to this, note that a pure Bloch state has $\mathcal{P}(\varepsilon_{\mathbf{k}}) = 1$ since its wave function is entirely localized at the point \mathbf{k} in the BZ).

* Corresponding author: vpereira@nus.edu.sg

¹ Q. H. Wang, K. Kalantar-Zadeh, A. Kis, J. N. Coleman, and M. S. Strano, *Nat. Nanotechnol.* **7**, 699 (2012).

² A. K. Geim and I. V. Grigorieva, *Nature* **499**, 419 (2013).

³ S. Z. Butler, S. M. Hollen, L. Cao, Y. Cui, J. A. Gupta, H. R. Gutierrez, T. F. Heinz, S. S. Hong, J. Huang, A. F. Ismach, E. Johnston-Halperin, M. Kuno, V. V. Plashnitsa, R. D. Robinson, R. S. Ruoff, S. Salahuddin, J. Shan, L. Shi, M. G. Spencer, M. Terrones, W. Windl, and J. E. Goldberger, *ACS Nano* **7**, 2898 (2013).

⁴ W. Choi, N. Choudhary, G. H. Han, J. Park, D. Akinwande, and Y. H. Lee, *Materials Today* **20**, 116 (2017).

⁵ G. Wang, A. Chernikov, M. M. Glazov, T. F. Heinz, X. Marie, T. Amand, and B. Urbaszek, [arXiv:1707.05863](https://arxiv.org/abs/1707.05863) (2017).

⁶ H.-P. Komsa and A. V. Krasheninnikov, *Phys. Rev. B* **86**, 241201 (2012).

⁷ G. Berghäuser and E. Malic, *Phys. Rev. B* **89**, 125309 (2014).

⁸ A. Molina-Sánchez, D. Sangalli, K. Hummer, A. Marini, and L. Wirtz, *Phys. Rev. B* **88**, 045412 (2013).

⁹ T. C. Berkelbach, M. S. Hybertsen, and D. R. Reichman, *Phys. Rev. B* **88**, 045318 (2013).

¹⁰ D. Y. Qiu, F. H. da Jornada, and S. G. Louie, *Phys. Rev. Lett.* **111**, 216805 (2013).

¹¹ M. L. Trolle, G. Seifert, and T. G. Pedersen, *Phys. Rev. B* **89**, 235410 (2014).

¹² C. Zhang, A. Johnson, C.-L. Hsu, L.-J. Li, and C.-K. Shih, *Nano Lett.* **14**, 2443 (2014).

- ¹³ F. Wu, F. Qu, and A. H. MacDonald, *Phys. Rev. B* **91**, 075310 (2015).
- ¹⁴ P. San-Jose, V. Parente, F. Guinea, R. Roldán, and E. Prada, *Phys. Rev. X* **6**, 031046 (2016).
- ¹⁵ A. J. Chaves, R. M. Ribeiro, T. Frederico, and N. M. R. Peres, *2D Mater.* **4**, 025086 (2017).
- ¹⁶ M. Trushin, M. O. Goerbig, and W. Belzig, *Journal of Physics: Conference Series* **864**, 012033 (2017).
- ¹⁷ M. Selig, G. Berghäuser, A. Raja, P. Nagler, C. Schiller, T. F. Heinz, T. Korn, A. Chernikov, E. Malic, and A. Knorr, *Nat. Commun.* **7**, 13279 (2016).
- ¹⁸ Z. Wang, Y. Xiao, W. Li, R.-Z. Li, and Z.-Q. Li, *arXiv:1701.00559* (2017).
- ¹⁹ M. Grüning and C. Attacalite, *Phys. Rev. B* **89**, 081102 (2014).
- ²⁰ M. M. Glazov, L. E. Golub, G. Wang, X. Marie, T. Amand, and B. Urbaszek, *Phys. Rev. B* **95**, 035311 (2017).
- ²¹ S. H. Rhim, Y. S. Kim, and A. J. Freeman, *Appl. Phys. Lett.* **107**, 241908 (2015).
- ²² C.-Y. Wang and G.-Y. Guo, *J. Phys. Chem. C* **119**, 13268 (2015).
- ²³ K. F. Mak, C. Lee, J. Hone, J. Shan, and T. F. Heinz, *Phys. Rev. Lett.* **105**, 136805 (2010).
- ²⁴ A. Splendiani, L. Sun, Y. Zhang, T. Li, J. Kim, C.-Y. Chim, G. Galli, and F. Wang, *Nano Lett.* **10**, 1271 (2010).
- ²⁵ Y. Li, Y. Rao, K. F. Mak, Y. You, S. Wang, C. R. Dean, and T. F. Heinz, *Nano Lett.* **13**, 3329 (2013).
- ²⁶ C. Zhang, H. Wang, W. Chan, C. Manolatou, and F. Rana, *Phys. Rev. B* **89**, 205436 (2014).
- ²⁷ Y. Li, A. Chernikov, X. Zhang, A. Rigosi, H. M. Hill, A. M. van der Zande, D. A. Chenet, E.-M. Shih, J. Hone, and T. F. Heinz, *Phys. Rev. B* **90**, 205422 (2014).
- ²⁸ K. P. Dhakal, D. L. Duong, J. Lee, H. Nam, M. Kim, M. Kan, Y. H. Lee, and J. Kim, *Nanoscale* **6**, 13028 (2014).
- ²⁹ J. A. Miwa, S. Ulstrup, S. G. Sørensen, M. Dendzik, A. G. Čabo, M. Bianchi, J. V. Lauritsen, and P. Hofmann, *Phys. Rev. Lett.* **114**, 046802 (2015).
- ³⁰ H. M. Hill, A. F. Rigosi, C. Roquelet, A. Chernikov, T. C. Berkelbach, D. R. Reichman, M. S. Hybertsen, L. E. Brus, and T. F. Heinz, *Nano Lett.* **15**, 2992 (2015).
- ³¹ A. R. Klots, A. K. M. Newaz, B. Wang, D. Prasai, H. Krzyzanowska, J. Lin, D. Caudel, N. J. Ghimire, J. Yan, B. L. Ivano, K. A. Velizhanin, A. Burger, D. G. Mandru, N. H. Tolk, S. T. Pantelides, and K. I. Bolotin, *Sci. Rep.* **4**, 6608 (2014).
- ³² A. F. Rigosi, H. M. Hill, K. T. Rim, G. W. Flynn, and T. F. Heinz, *Phys. Rev. B* **94**, 075440 (2016).
- ³³ S. H. Aleithan, M. Y. Livshits, S. Khadka, J. J. Rack, M. E. Kordesch, and E. Stinaff, *Phys. Rev. B* **94**, 035445 (2016).
- ³⁴ M.-H. Chiu, C. Zhang, H.-W. Shiu, C.-P. Chuu, C.-H. Chen, C.-Y. S. Chang, C.-H. Chen, M.-Y. Chou, C.-K. Shih, and L.-J. Li, *Nat. Commun.* **6**, 7666 (2015).
- ³⁵ N. Kumar, S. Najmaei, Q. Cui, F. Ceballos, P. M. Ajayan, J. Lou, and H. Zhao, *Phys. Rev. B* **87**, 161403 (2013).
- ³⁶ D. J. Clark, V. Senthilkumar, C. T. Le, D. L. Weerawarne, B. Shim, J. I. Jang, J. H. Shim, J. Cho, Y. Sim, M.-J. Seong, S. H. Rhim, A. J. Freeman, K.-H. Chung, and Y. S. Kim, *Phys. Rev. B* **90**, 121409 (2014).
- ³⁷ E. Mishina, N. Sherstyuk, S. Lavrov, A. Sigov, A. Mitioğlu, S. Anghel, and L. Kulyuk, *Appl. Phys. Lett.* **106**, 131901 (2015).
- ³⁸ M. L. Trolle, Y.-C. Tsao, K. Pedersen, and T. G. Pedersen, *Phys. Rev. B* **92**, 161409 (2015).
- ³⁹ A. Säynätjoki, L. Karvonen, H. Rostami, A. Autere, S. Mehravar, A. Lombardo, R. A. Norwood, T. Hasan, N. Peyghambarian, H. Lipsanen, K. Kieu, A. C. Ferrari, M. Polini, and Z. Sun, *Nat. Commun.* **8**, 893 (2016).
- ⁴⁰ R. I. Woodward, R. T. Murray, C. F. Phelan, R. E. P. de Oliveira, T. H. Runcorn, E. J. R. Kelleher, S. Li, E. C. de Oliveira, G. J. M. Fechine, G. Eda, and C. J. S. de Matos, *2D Mater.* **4**, 011006 (2017).
- ⁴¹ X. Yin, Z. Ye, D. A. Chenet, Y. Ye, K. O'Brien, J. C. Hone, and X. Zhang, *Science* **344**, 488 (2014).
- ⁴² S. Zhang, N. Dong, N. McEvoy, M. O'Brien, S. Winters, N. C. Berner, C. Yim, Y. Li, X. Zhang, Z. Chen, L. Zhang, G. S. Duesberg, and J. Wang, *ACS Nano* **9**, 7142 (2015).
- ⁴³ F. Liu, J. Zhou, C. Zhu, and Z. Liu, *Adv. Funct. Mater.* **27**, 1602404 (2017).
- ⁴⁴ Y. Saito, T. Nojima, and Y. Iwasa, *Supercond. Sci. Technol.* **29**, 93001 (2016).
- ⁴⁵ F. Wang, Z. Wang, Q. Wang, F. Wang, L. Yin, K. Xu, Y. Huang, and J. He, *Nanotechnology* **26**, 292001 (2015).
- ⁴⁶ A. Raja, A. Chaves, G. A. Jaeun Yu, H. M. Hill, A. F. Rigosi, T. C. Berkelbach, P. Nagler, C. Schüller, T. Korn, C. Nuckolls, J. Hone, L. E. Brus, T. F. Heinz, D. R. Reichman, and A. Chernikov, *Nat. Commun.* **8**, 15251 (2017).
- ⁴⁷ S. Nakajima, Y. Toyozawa, and R. Abe, *The physics of elementary excitations* (Springer-Verlag, Berlin, New York, 1980).
- ⁴⁸ R. Roldán, L. Chirulli, E. Prada, J. A. Silva-Guillén, P. San-Jose, and F. Guinea, *Chem. Soc. Rev.* **46**, 4387 (2017).
- ⁴⁹ M. Ugeda, A. Bradley, S.-F. Shi, F. H. da Jornada, Y. Zhang, D. Qiu, W. Ruan, S. Mo, Z. Hussain, Z.-X. Shen, F. Wang, S. Louie, and M. Crommie, *Nature Materials* **13**, 1091 (2014).
- ⁵⁰ D. Xiao, G.-B. Liu, W. Feng, X. Xu, and W. Yao, *Phys. Rev. Lett.* **108**, 196802 (2012).
- ⁵¹ K. F. Mak, K. He, J. Shan, and T. F. Heinz, *Nat. Nanotechnol.* **7**, 494 (2012).
- ⁵² H. Zheng, J. Dai, W. Yao, D. Xiao, and X. Cui, *Nature Nano* **7**, 490 (2012).
- ⁵³ G. Sallen, L. Bouet, X. Marie, G. Wang, C. R. Zhu, W. P. Han, Y. Lu, P. H. Tan, T. Amand, B. L. Liu, and B. Urbaszek, *Phys. Rev. B* **86**, 081301 (2012).
- ⁵⁴ T. Cao, G. Wang, W. Han, H. Ye, C. Zhu, J. Shi, Q. Niu, P. Tan, E. Wang, B. Liu, and J. Feng, *Nat. Commun.* **3**, 887 (2012).
- ⁵⁵ L. Bawden, S. P. Cooil, F. Mazzola, J. M. Riley, L. J. Collins-McIntyre, V. Sunko, K. W. B. Hunvik, M. Leandersson, C. M. Polley, T. Balasubramanian, T. K. Kim, M. Hoesch, J. W. Wells, G. Balakrishnan, M. S. Bahramy, and P. D. C. King, *Nat. Commun.* **7**, 11711 (2016).
- ⁵⁶ J. Zhou, W. Y. Shan, W. Yao, and D. Xiao, *Phys. Rev. Lett.* **115**, 166803 (2015).
- ⁵⁷ A. Srivastava and A. Imamoğlu, *Phys. Rev. Lett.* **115**, 166802 (2015).
- ⁵⁸ M. Rohlfing and S. G. Louie, *Phys. Rev. B* **62**, 4927 (2000).
- ⁵⁹ E. Ridolfi, D. Le, T. S. Rahman, E. R. Mucciolo, and C. H. Lewenkopf, *J. Phys.: Condens. Matter* **27**, 365501 (2015).
- ⁶⁰ A. Ramasubramaniam, *Phys. Rev. B* **86**, 115409 (2012).
- ⁶¹ A. Molina-Sánchez, M. Palumbo, A. Marini, and L. Wirtz, *Phys. Rev. B* **93**, 155435 (2016).
- ⁶² S. Tongay, J. Zhou, C. Ataca, K. Lo, T. S. Matthews, J. Li, J. C. Grossman, and J. Wu, *Nano Lett.* **12**, 5576 (2012).

- ⁶³ G. Kioseoglou, A. Hanbicki, M. Currie, A. Friedman, and B. Jonker., *Sci. Rep.* **6**, 25041 (2016).
- ⁶⁴ For example, Ref. 10 attributes the peak C to transitions near, but not directly at, the Γ point, which require a fine sampling with 300^2 \mathbf{k} points, and at least 56 bands in the underlying GW calculation. The authors also use local field effects to include the interaction over different BZs.
- ⁶⁵ P. Cudazzo, I. V. Tokatly, and A. Rubio, *Phys. Rev. B* **84**, 085406 (2011).
- ⁶⁶ A. Chernikov, T. C. Berkelbach, H. M. Hill, A. Rigosi, Y. Li, O. B. Aslan, D. R. Reichman, M. S. Hybertsen, and T. F. Heinz, *Phys. Rev. Lett.* **113**, 076802 (2014).
- ⁶⁷ A. S. Rodin, A. Carvalho, and A. H. Castro Neto, *Phys. Rev. B* **90**, 075429 (2014).
- ⁶⁸ L. V. Keldysh, *JETP Lett.* **29**, 658 (1979).
- ⁶⁹ N. Saigal, V. Sugunakar, and S. Ghosh, *Appl. Phys. Lett.* **108**, 132105 (2016).
- ⁷⁰ E. E. Salpeter and H. A. Bethe, *Phys. Rev.* **84**, 1232 (1951).
- ⁷¹ <http://www.bethe-salpeter.org>.
- ⁷² S. Albrecht, L. Reining, R. Del Sole, and G. Onida, *Phys. Rev. Lett.* **80**, 4510 (1998).
- ⁷³ J. Li, M. Holzmann, I. Duchemin, X. Blase, and V. Olevano, *Phys. Rev. Lett.* **118**, 163001 (2017).
- ⁷⁴ G. Grosso and G. P. Parravicini, *Solid State Physics* (Elsevier Science, Oxford, 2014).
- ⁷⁵ For the derivation of the BSE in details on the computation of W see, for instance, Chapters VII.1. and IV.4-5 of Ref. 74.
- ⁷⁶ S. Latini, T. Olsen, and K. S. Thygesen, *Phys. Rev. B* **92**, 245123 (2015).
- ⁷⁷ The expression $r_0 = \frac{\epsilon_2 d}{\epsilon_1 + \epsilon_3}$ is sometimes reported as the limit of Eq. (10) when $\epsilon_2 \gg \epsilon_{1,3}$.
- ⁷⁸ F. M. Hipolito, *On linear and non-linear interactions of light with two dimensional materials*, Ph.D. thesis, National University of Singapore (2016).
- ⁷⁹ Having $\alpha_1 = 1$, $\alpha_{2,3} = 0$ in Eq. (17) corresponds to leaving the factor $\propto 1/\kappa(q)$ in the potential (8) outside of the average integral.
- ⁸⁰ Recall that if $N_k = 100$, the full diagonalization of the BSE Hamiltonian requires handling a matrix of dimension $N_{\text{tot}} \times N_{\text{tot}} = (10^4 N_c N_v)^2$. For us, with $N_c = 8$ and $N_v = 2$, that amounts to $\simeq 2.56 \times 10^{10}$.
- ⁸¹ In particular, #11 consists of choosing $q=0$ at the center of a square integration domain of side $2\pi/aN_k$ and #2 in placing $q=0$ at the corner of the same integration square.
- ⁸² M. R. Molas, C. Faugeras, A. O. Slobodeniuk, K. Nogajewski, M. Bartos, D. M. Basko, and M. Potemski, *2D Mater.* **4**, 021003 (2017).
- ⁸³ J. P. Echeverry, B. Urbaszek, T. Amand, X. Marie, and I. C. Gerber, *Phys. Rev. B* **93**, 121107(R) (2016).
- ⁸⁴ M. Baranowski, A. Surrente, D. K. M. M. Ballottin, A. Mitoglu, P. Christianen, Y. Kung, D. Dumcenco, A. Kis, and P. Plochocka, *2D Mater.* **4**, 025016 (2017).
- ⁸⁵ E. Malic, M. Selig, M. Feierabend, S. Brem, D. Christiansen, F. Wendler, A. Knorr, and G. Berghuser, *Phys. Rev. Materials* **2**, 014002 (2018).
- ⁸⁶ X. Zhang, T. Cao, Z. Lu, Y. Lin, F. Zhang, Y. Wang, Z. Li, J. Hone, J. Robinson, D. Smirnov, S. Louie, and . Tony F. Heinz2, *Nat. Nanotechnol.* **12**, 883888 (2017).
- ⁸⁷ Alternatively, the experimental positions of the A and B peaks can be matched by tuning the environment dielectric constants that determine r_0 [cf. Eq. (10)]¹¹.
- ⁸⁸ G. Jayaswal, Z. Dai, X. Zhang, M. Bagnarol, A. Martucci, and M. Merano, *Opt. Lett.* **43**, 703 (2018).
- ⁸⁹ The results for the B excitons are not shown explicitly, but are similar to those reported in Fig. 5 for the A counterparts.
- ⁹⁰ A. Molina-Sánchez, K. Hummer, and L. Wirtz, *Surf. Sci. Rep.* **70**, 554 (2015).
- ⁹¹ At a technical level, it is important to realize that the sharp localization associated with the C excitons requires a fine \mathbf{k} -point mesh to ensure proper convergence of the absorption spectrum over this large range of energies 10.
- ⁹² L. M. Malard, T. V. Alencar, A. P. M. Barboza, K. F. Mak, and A. M. de Paula, *Phys. Rev. B* **87**, 201401 (2013).
- ⁹³ E. Cappelluti, R. Roldán, J. A. Silva-Guillén, P. Ordejón, and F. Guinea, *Phys. Rev. B* **88**, 75409 (2013).
- ⁹⁴ We stress, however, that some models require rather large rigid shifts in energy and/or vertical scaling in order to make the calculated results agree with the experimental traces as shown in Fig. 7.
- ⁹⁵ For completeness, it is worth noting that the spectral shape in the range of the C excitons measured in MoS₂ multilayers changes appreciably with layer number, as shown by the experiments reported in Ref. 28.